Journal of Human Genetics (2018) 63:1211–1222
https://doi.org/10.1038/s10038-018-0515-y

ARTICLE

Biallelic mutations in FDXR cause neurodegeneration associated with inflammation

Jesse Slone[1] · Yanyan Peng[1] · Adam Chamberlin[2] · Belinda Harris[3] · Julie Kaylor[4] · Marie T. McDonald[5] · Monica Lemmon[5] · Mays Antonine El-Dairi[6] · Dmitry Tchapyjnikov[5] · Laura A Gonzalez-Krellwitz[7] · Elizabeth A. Sellars[4] · Allyn McConkie-Rosell[5] · Laura G. Reinholdt[3] · Taosheng Huang[1,8]

Received: 1 May 2018 / Revised: 24 August 2018 / Accepted: 26 August 2018 / Published online: 25 September 2018

Abstract

Mitochondrial dysfunction lies behind many neurodegenerative disorders, owing largely to the intense energy requirements of most neurons. Such mitochondrial dysfunction may work through a variety of mechanisms, from direct disruption of the electron transport chain to abnormal mitochondrial biogenesis. Recently, we have identified biallelic mutations in the mitochondrial flavoprotein "ferredoxin reductase" (*FDXR)* gene as a novel cause of mitochondriopathy, peripheral neuropathy, and optic atrophy. In this report, we expand upon those results by describing two new cases of disease-causing *FDXR* variants in patients with variable severity of phenotypes, including evidence of an inflammatory response in brain autopsy. To investigate the underlying pathogenesis, we examined neurodegeneration in a mouse model. We found that *Fdxr* mutant mouse brain tissues share pathological changes similar to those seen in patient autopsy material, including increased astrocytes. Furthermore, we show that these abnormalities are associated with increased levels of markers for both neurodegeneration and gliosis, with the latter implying inflammation as a major factor in the pathology of *Fdxr* mutations. These data provide further insight into the pathogenic mechanism of FDXR-mediated central neuropathy, and suggest an avenue for mechanistic studies that will ultimately inform treatment.

Introduction

Neurons require a steady supply of cellular energy in order to function, and disruptions in cellular metabolism are associated with many diseases of the nervous system. Mitochondrial disorders are particularly common causes of neural disorders, given the central role of oxidative phosphorylation in cellular ATP production. This association is readily apparent when one examines many of the classic disease-causing mutations in the mitochondrial genome, which underlie a variety of neurological and neuromuscular disorders such as MERFF (myoclonic epilepsy and ragged-red fiber disease) [1], NARP (neuropathy, ataxia, and retinitis pigmentosa) [2], and MELAS (mitochondrial myopathy, encephalopathy, lactic acidosis, and stroke-like episodes) [3]. Moreover, although primary mitochondrial disorders such as those listed above are relatively rare, mitochondrial dysfunction is known to play a role in a variety of common diseases, including neurodegenerative disorders like Parkinson's and Alzheimer's disease [4]. For this reason, the study of primary mitochondrial disorders is of great importance to the medical field, as they may reveal

✉ Taosheng Huang
Taosheng.Huang@cchmc.org

1 Division of Human Genetics, Children's Hospital Medical Center, Cincinnati, OH, USA45229

2 Ambry Genetics, Aliso Viejo, CA, USA92656

3 The Jackson Laboratory, Bar Harbor, ME, USA04609

4 University of Arkansas for Medical Sciences, Section of Genetics and Metabolism, 1 Children's Way, Little Rock, AR, USA72202

5 Department of Pediatrics, Duke University School of Medicine, Durham, NC, USA27710

6 Department of Ophthalmology, Duke University School of Medicine, Durham, NC, USA27710

7 Department of Pathology, Arkansas Children's Hospital, 1 Children's Way, Little Rock, AR, USA72202

8 Human Aging Research Institute, Nanchang University, Nanchang, China

mechanistic insights with broader application to these more common diseases.

Neurodegenerative disorders linked to mitochondrial dysfunction are likely caused by mutations in a variety of nuclear and mitochondrial loci, many of which have already been identified. One particularly well-studied example is the mitochondrial protein *frataxin*, which has been shown to be the causative agent behind Friedreich's ataxia, the most common form of inherited ataxia. Although the precise functions of *frataxin* remain unclear, it has been shown to be required for the synthesis of iron–sulfur clusters [5]. Mitochondria are the primary location for iron–sulfur cluster synthesis [6], and multiple mitochondrial disorders have already been linked to defective iron–sulfur cluster synthesis [7, 8]. In the case of *frataxin*, loss of its activity leads to both a reduction in iron–sulfur cluster production and an increase in mitochondrial iron levels [9]. The latter effect is particularly toxic to the cell, as iron buildup in the mitochondria accelerates reactive oxygen species (ROS) production and enhances oxidative stress. For this reason, there is great interest in investigating the role other iron metabolism genes may play in causing neurodegenerative disorders.

Our laboratory has previously used whole-exome sequencing (WES) of 17 patients from 13 different families to identify mutations in the *FDXR* gene as a novel cause of mitochondrial dysfunction leading to neuropathy, optic atrophy, ataxia, hypotonia, and global developmental delay [10]. In parallel, work from another group also showed that mutations in the *ferredoxin reductase* gene (FDXR) lead to peripheral sensory neuropathy in eight subjects from four different patient families [11]. Additional experiments in yeast and in patient fibroblasts indicated that these defects may be due to misregulation of iron homeostasis in the cell. Prior to this, FDXR had been known to be required for cell viability, and to suppress the growth of colon cancer cells (likely through the induction of mitochondrial oxidative stress) in a p53-dependent manner [12]. FDXR's main function within the cell appears to be its role in the assembly of iron–sulfur clusters, where it facilitates the transfer of electrons from nicotinamide adenine dinucleotide phosphate (NADPH) to the ferredoxins FDX1 and FDX2 [5, 13–16]. FDX1 and FDX2, in turn, donate their electrons for Fe–S cluster assembly [14, 16], or pass them on to mitochondrial cytochromes P450 (CYP) [17], which are involved in drug metabolism [18] and steroid synthesis pathways [19], among other important functions. This places FDXR at the nexus of several pathways critical to the normal functioning of both the mitochondria and the cell as a whole.

Our initial studies in patient-derived fibroblasts revealed the general mechanism for FDXR's role in neurodegenerative mitochondriopathy, showing that loss of FDXR function leads to decreased ferredoxin NADP reductase activity; reduced function of complexes I, II, and III in the electron transport chain; and a significant increase in reactive oxygen species (ROS) production by the patient cells [10]. All three mechanisms are likely to be major factors in the pathology of the disease, although loss of iron–sulfur cluster production and dysregulated iron metabolism are likely to be important players as well.

Here, we have examined two new patient cases of compound heterozygous mutations in *FDXR*. These cases further expand the clinical and genetic spectrum of the disease and confirm that disruption of FDXR function leads to severe visual defects and optic atrophy, as well as atrophy of the cerebellum and cerebral cortex. Taking advantage of our previously characterized, naturally occurring mouse model with homozygous *Fdxr* mutations, we demonstrate that *FDXR* mutations cause a striking increase in markers of both neurodegeneration and glial activation. As glial activation is known to be closely associated with inflammatory responses in the central nervous system, these results strongly implicate inflammation as an important pathological mechanism in this disease model. This finding provides a new and promising avenue for future research into the causes and treatments for patients carrying FDXR mutations, as well as similar forms of neurodegenerative disease.

Materials and methods

Human subjects

The study was approved by Cincinnati Children's Hospital IRB and an informed consent was obtained from each of the families.

Animal models

All procedures involving mice were approved by The Jackson Laboratory's Institutional Animal Care and Use Committee and performed in accordance with the National Institutes of Health guidelines for the care and use of animals in research. The strain used for this study was B6;129S-*Fdxr*^{m1J}*Otop3*^{m1J}/GrsrJ (The Jackson Laboratory stock, #026096). Although this strain carries a second mutation in the *Otop3* gene, this allele is unlikely to contribute to the phenotype observed here, as targeted deletion of *Otop3* results in a different phenotype (increased startle reflex and oligodactyly) than is observed with our homozygous *Fdxr* mutants.

WES

For both families, proband-parent trio WES was performed as described previously [10]. In brief, blood was collected

from the patient and his/her parents, and genomic DNA was extracted and purified. For Family 2, blood samples were also collected from the proband's sibling. The exon targets were captured using a Clinical Research Exome kit (Agilent Technologies, Santa, CA). The sequencing technology and variant interpretation protocol employed are described elsewhere [20].

Hematoxylin and eosin (H&E) staining

Tissues were fixed in 10% formaldehyde and then embedded in paraffin. Sections were cut and then stained with H&E. Images were obtained under light microscopy (BX63; Olympus Corporation; Center Valley, PA) as described before [10, 21].

Immunohistochemistry (IHC)

Tissues were fixed in 4% paraformaldehyde (in phosphate-bufffered saline (PBS)) and stored at 4 °C for 24–72 h. Tissues were then transferred to 30% sucrose for long-term storage at 4 °C. In preparation for IHC, tissues were frozen in OCT-embedding medium, and then cut into 10-micron sections with a cryostat. To detect gliosis, tissues were stained with anti-glial fibrillary acidic protein (anti-GFAP) antibody. Staining with anti-NeuN was used to detect the presence of neurons, with 4′,6-diamidino-2-phenylindole as a counterstain to detect total number of nuclei. The detailed procedure was described before [10, 21].

Fluoro-Jade C (FJC) staining

Frozen sections were mounted on gelatin-coated slides, air-dried, and subjected to FJC staining [21]. Slides were immersed in a solution containing 1% NaOH in 80% ethanol for 5 min, rinsed in 70% ethanol for 2 min, rinsed in distilled water for 2 min, and incubated in 0.06% potassium permanganate solution for 10 min. Following a water rinse for 2 min, slides were transferred to 0.0001% FJC (MILLIPORE, AG325) staining solution dissolved in 0.1% acetic acid for 10 min. After three washings with water, slides were air-dried on a slide warmer at 50 °C for 30 min, then cleared in xylene and cover-slipped with DPX (Sigma-Aldrich), a mixture of distyrene, a plasticizer, and xylene used as a mounting media. Signals were visualized with a Zeiss Axiovert 200 M microscope.

Electron microscopy

Electron microscopy was performed as described previously [21]. In short, mice were killed and perfused with electron microscope (EM) fixative in saline solution (4% paraformaldehyde, 2.5% glutaraldehyde, PBS, pH 7.4–7.6). The relevant tissues were extracted and postfixed in EM fixative buffer, washed in 0.1 M Na cacodylate buffer (EMS, Hatfield, PA), and treated with 1% osmium tetroxide (EMS) for 1 h at 4 °C. Samples were washed in 0.1 M Na cacodylate buffer and dehydrated through a graded ethanol series and embedded in LX-112 (Ladd Research Industries, Williston, VT). Tissue blocks were sectioned to a thickness of 0.5–1 microns, stained with toluidine blue, and examined by light microscopy before further processing. After checking the tissues by light microscopy, blocks were cut and trimmed with an ultramicrotome (Leica EM UC7, Buffalo Grove, IL) to a 90-nm thickness. Sections were counterstained with uranyl acetate 2% (EMS) and lead citrate, and then examined by transmission electron microscopy (TEM). All TEM images were taken with an 80-kV transmission electron microscope (Hitachi, H-7650, V01.07, Tokyo, Japan).

Optical coherence tomography (OCT)

Handheld Bioptigen spectral domain optical coherence tomography was performed on the proband of family 1 at the age of 35 months. OCT was performed while the patient was awake, on the fovea in both eyes.

Autopsy

Autopsy was performed on proband 2 at the age of 10.5 months. External examination was conducted to determine weight, length, and gross anatomical features. We performed histological analysis and examination by TEM on the heart and lungs, the occipital cerebral cortex and cerebellar cortex.

Results

Case #1

The proband of this family was born prematurely at 29 weeks, to non-consanguineous parents. The proband was born via emergency cesarean section in response to maternal pre-eclampsia. This was followed by 2 months spent in the neonatal intensive care unit. Early in life, he was noted to have global developmental delay, with delays in speech, fine motor, and gross motor skills. At ~2 years of age, he developed the sudden onset of ataxia and refusal to bear weight in the setting of a recent febrile upper respiratory infection. Lumbar puncture and magnetic resonance imaging (MRI) of the brain and spine were normal at that time. Although his ataxia initially improved with the help of physical therapy, he continued to experience episodes of intermittent ataxia, ultimately developing a persistent gait

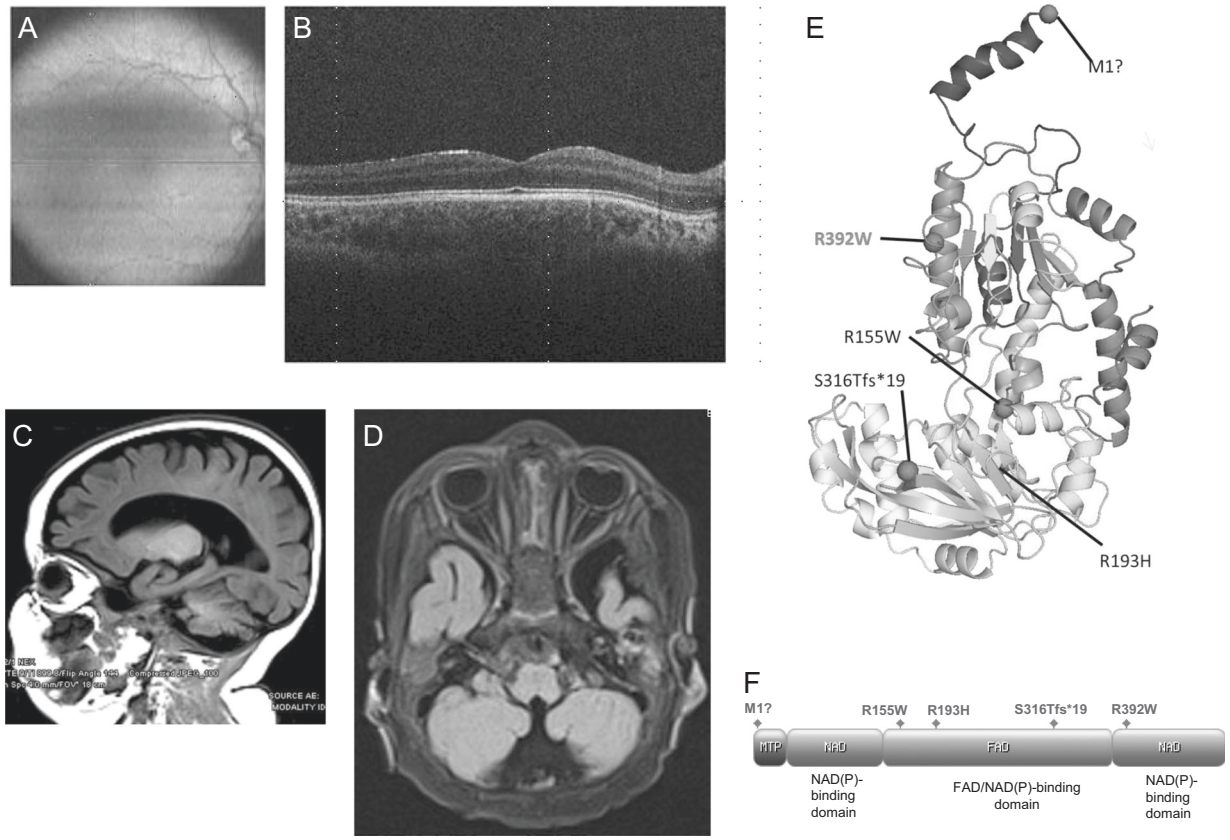

Fig. 1 Optic atrophy and cerebral atrophy in patients carrying biallelic mutations in *FDXR*. **a–b** Optical coherence tomography (OCT) of retina from the proband of Family #1. Images were obtained at the age of 35 months. The green line shown in the fundus photograph in panel **a** indicates the position of the OCT scan shown in **b**. The fovea appears to be well-formed, and the outer retinal layers are normal. The inner retina, however, shows almost complete absence of the ganglion cell layer in both eyes and severe thinning of the nerve fiber layer, consistent with bilateral optic atrophy involving the papillomacular bundle. **c–d** MRI images from the proband of Family #2 also show optic nerve hypoplasia **c** and global cerebral atrophy with marked prominence of sulci and ventricles **d**. **e** Patient mutations were mapped to a three-dimensional FDXR protein structure model. The most common variant observed in all patient families (R392W) [10] has been highlighted in red for comparison. **f** Patient mutations were also mapped to a two-dimensional map of the FDXR functional domains. Domain map was generated using the "MyDomains" software provided by PROSITE [34]

abnormality. Neurologic exam was notable for speech delay, axial hypotonia, and ataxic gait.

The patient was additionally found to have nystagmus and poor vision. Ophthalmic examination showed vision was 20/600 (legal blindness) in each eye, but the visual fields were full to confrontation. The optic nerves were normal in size, but there was bilateral optic nerve atrophy causing central scotomas. Optical coherence tomography showed severe thinning of the ganglion cell layer in the papillomacular bundle area (Fig. 1a–b).

A proband-parent trio WES was performed to determine the cause of the patient's condition. Although this analysis was initially inconclusive, the patient was found to be carrying *FDXR* variants of uncertain pathogenicity. These variants were later reclassified as likely pathogenic variants when other patients carrying *FDXR* mutations began to come to light [10, 11], with many of them showing symptoms similar to the proband's. In the proband's case, he has been determined to be compound heterozygous for a known pathogenic variant (c.1A > G, p.M1?) and a likely pathogenic variant (c.463C > T, p.R155W) of *FDXR*. Sequencing also confirmed that the parents are carriers of *FDXR* mutant variants. The clinically unaffected sibling was also examined and found to be a heterozygous carrier of only the c.463C > T, p.R155W variant. This suggests an autosomal recessive, loss-of-function, inheritance pattern for these variants, which agrees with our previous observations for FDXR mutations.

The patient is currently 3 years and 10 months old and has continued to gain skills. He has had no regression and no occurrences of seizures. He continues to have an ataxic gait; however, is ambulatory with the aid of orthotics. He speaks in 3–4 word phrases. He receives speech, occupational, and physical therapy. Repeat brain and orbit MRI at ~ 3 years of age was notable for bilateral optic atrophy. His phenotype suggests that the compound heterozygous variants carried by this patient are less severe than those observed in other variants such as p.S316Tfs*19 and p.

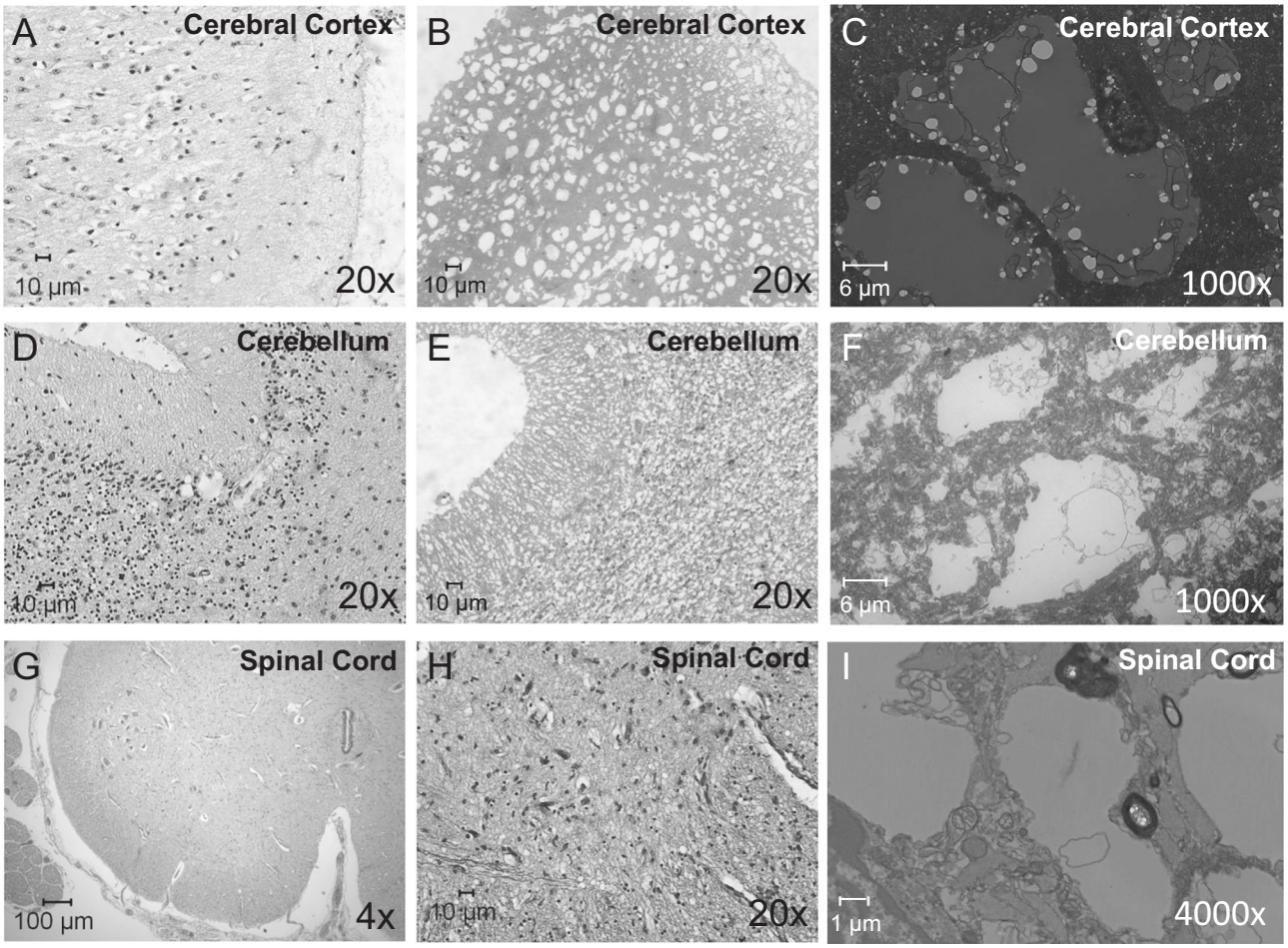

Fig. 2 Atrophy and cell loss in the CNS of the patient autopsy (proband 2) with *FDXR* mutations. Histological sectioning of the occipital cerebral cortex with H&E staining **a** indicated that the cerebral cortex lost many of its neurons, and multiple vacuoles were observed in the H&E staining section that formed a spongiform structure. Toluidine staining of the cerebral section **b** also showed the presence of spongiform-like structures in the cerebral cortex, and TEM confirmed this was largely due to the presence of vacuole-like structures **c**. The cerebellum of the patient also lost neurons in the molecular layer, Purkinje cell layer, and granular layer **d**–**f**. Most of the Purkinje cells were absent, and multiple vacuoles were observed with H&E staining **d**. Toluidine staining **e** and TEM imaging **f** of the cerebellar sections also showed loss of cells and the formation of vacuoles in the cerebellum. H&E staining **g**, **h** of spinal cord also indicated that the spinal cord lost lower motor neurons in the anterior horn **g**, and multiple vacuoles were formed in the spinal cord by H&E staining **h** and TEM **i**

R193H (described in Case #2 below), or the p.R392W variant found in the plurality (42.3%) of our previously reported patients [10].

Case #2

The second proband described in our study was unrelated to proband 1. She was born prematurely at 30–6/7 weeks' gestation by cesarean section because of worsening maternal hypertension. Her birth weight was 1130 grams and Apgar scores were 4/8/9. At birth, she presented with ambiguous genitalia, labial fusion, and clitoromegaly. Chromosomal analysis showed normal 46, XX. She then spent 2.5 months in neonatal intensive care unit for poor feeding, abdominal distension, and initial respiratory distress syndrome. Ophthalmology evaluation found small optic nerves. An MRI of head and orbits at the age of 2 months old showed bilateral thin optic nerves and cerebellar vermis hypoplasia. Ocular globes were normal in morphology; the pituitary gland was also normal. At 4 months of age, she was found to have bilateral cataracts and a urogenital sinus. Abdominal ultrasound revealed normal kidneys, normal bladder, and normal-appearing uterus with gonads. At 7 months old, she had a diagnostic laparoscopy with cystoscopy and gonadal biopsy as an outpatient procedure. Her gonadal biopsy showed immature ovarian parenchyma bilaterally. She was hospitalized owing to lethargy, *Klebsiella* urosepsis and enteroviral meningitis. She also presented with failure to thrive, global developmental delay, and muscular hypertonicity. During her hospitalization, she had a few episodes of apnea and experienced an anoxic event. MRI/MRS findings at that

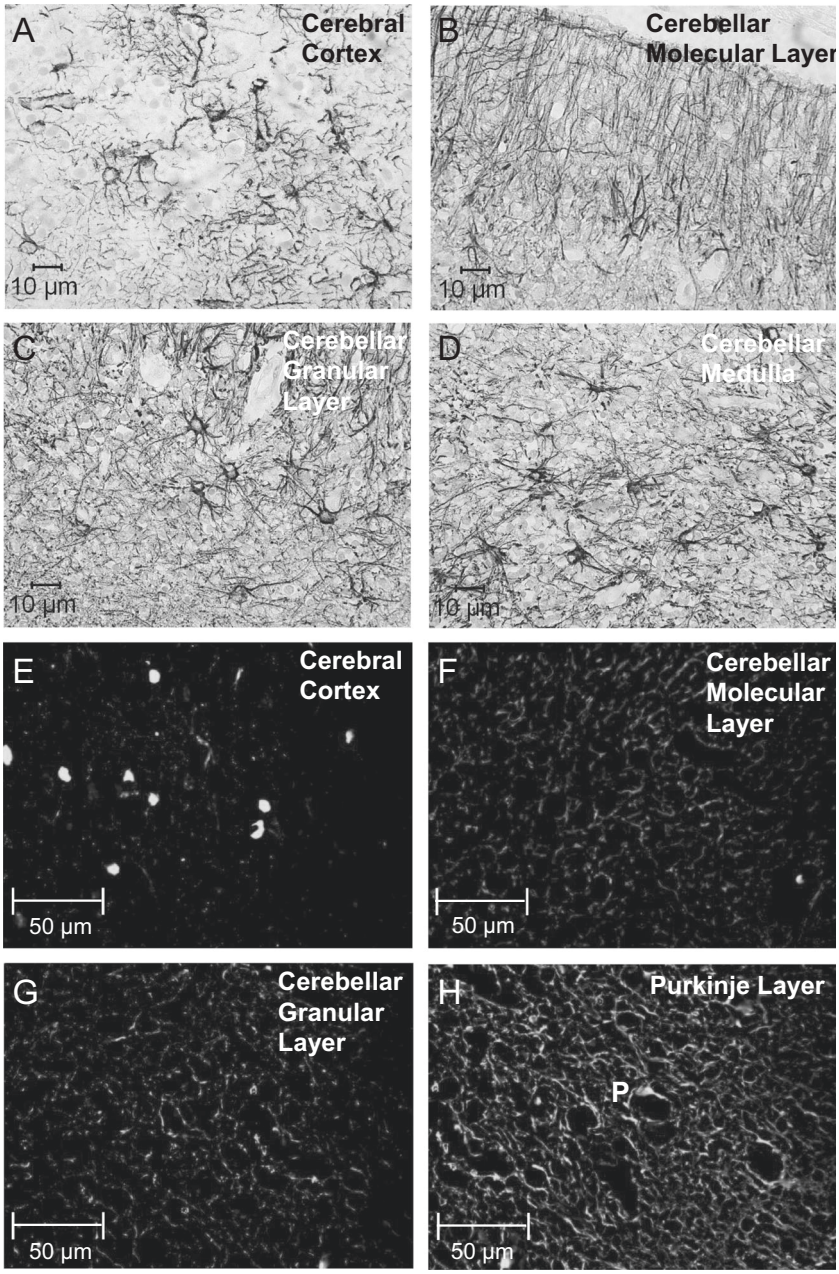

Fig. 3 Signs of gliosis and neurodegeneration in the autopsy brain from proband 2. Immunostaining with antibody specific for GFAP revealed extensive gliosis in the cerebral cortex **a**, as well as in the molecular layer **b**, granular layer **c**, and medullary layer **d** of the cerebellum. Astrocytes and their extending branches were observed throughout the cerebrum and cerebellum, and Bergmann glial cells were prominent throughout the molecular layer **b**. Immunostaining for Fluoro-Jade C (FJC) also showed signs of neurodegeneration in the cerebral cortex **e**, the cerebellar molecular layer **f**, the cerebellar granular layer **g**, and in the Purkinje layer **h**, Purkinje cell indicated by the letter "P")

time showed diminished size of the optic nerves and chiasm and global cerebral atrophy (Fig. 1c–d). An electroencephalography recorded overnight at 7 months old was normal. At 8 months, she developed an acute respiratory failure and was incubated with supportive care. Microarray results and sex-determining region Y fluorescence in situ hybridization were normal. Her extensive endocrine evaluation did not reveal etiology or diagnosis. A large exome slice focusing on disorders of sex development-related genes was normal.

Like Case #1, the parents were not consanguineous, and the genetic cause of the proband's condition was not initially apparent. Given the lack of obvious genetic causes, we performed a proband-parent trio WES. The WES of the patient's DNA revealed that the proband was compound heterozygous at the *FDXR* locus, with a c.947delG (p.S316Tfs*19) frameshift variant inherited from her mother and a c.578G > A (p.R193H) variant from her father.

The patient passed away at 10.5 months of age, and an autopsy was performed. At the time of autopsy (limited to chest, abdomen, and left posterior brain), proband 2 was small for the given age of 10.5 months with weight, length, and a head circumference of less than the 5th percentile, and showed mild generalized edema. Additional external findings

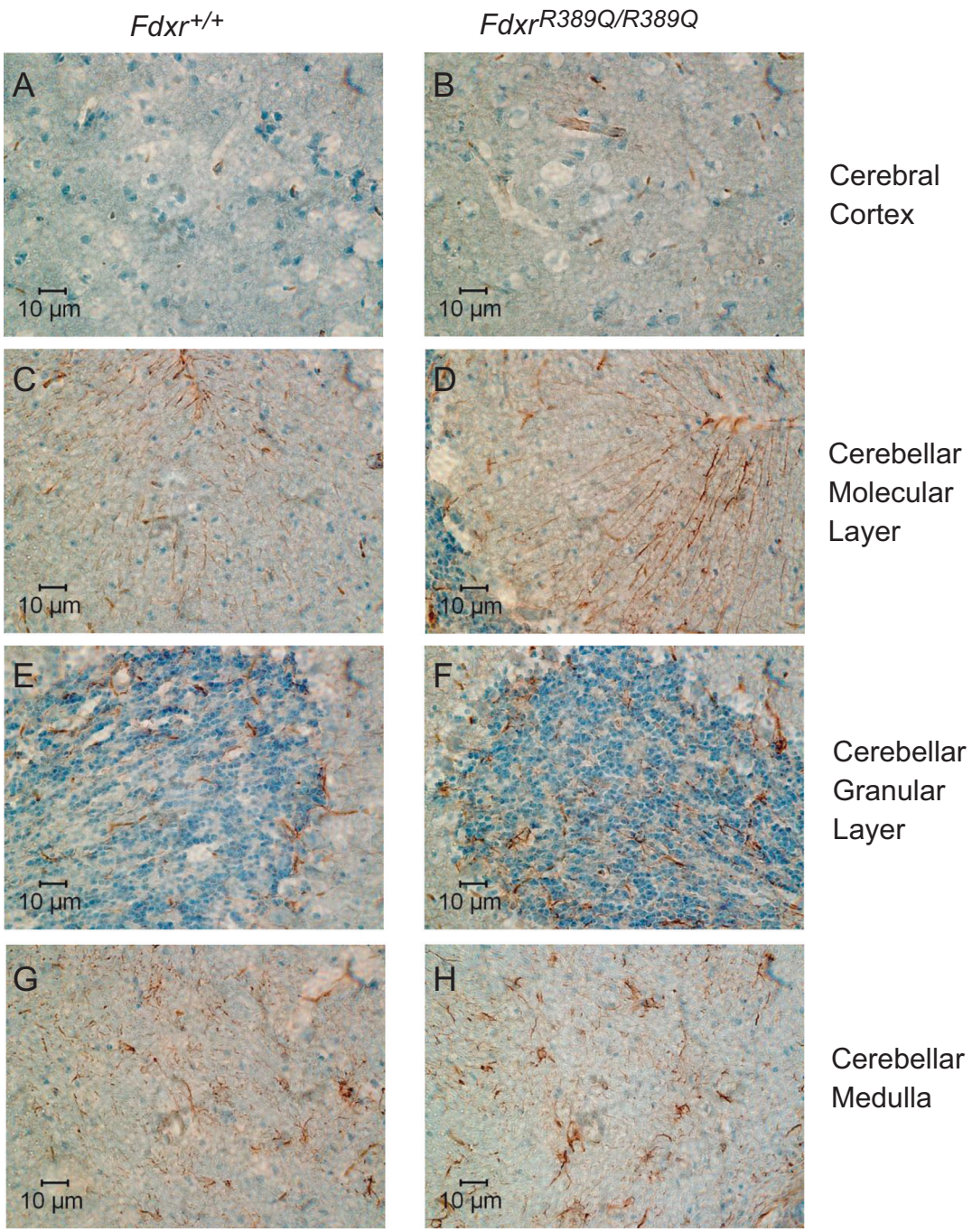

Fig. 4 Astrocyte gliosis in brains of mice with *Fdxr* gene mutation. Ten-month-old mouse mutant (*Fdxr* $^{R389Q/R389Q}$) and wildtype control brains were stained with anti-GFAP antibody, and images were compared for the cerebral cortex **a**–**b**, as well as the molecular layer **c**–**d**, granular layer **e**–**f**, and medullary layer **g**–**h** of the cerebellum. A modestly increased presence of astrocytes and Bergmann glial cells are apparent in the various layers of the cerebellum **c**–**h** and the cerebral cortex **a**–**b**

showed a prominent clitoral hood, clitoromegaly, and labial fusion. Internal examination demonstrated features of right-sided congestive heart failure, specifically dilated right atrial and ventricular chambers with dysplastic tricuspid valve leaflets, hepatosplenomegaly, and marked pulmonary congestion and edema. This was supported by microscopic evidence of chronic ischemia/hypoxemia with multifocal, remote right ventricular myocardial infarctions, pulmonary arteriopathy with near luminal occlusion, and extramedullary hematopoiesis identified in the left epicardium and thymus. The lungs revealed chronic lobular remodeling with alveolar simplification, moderate-to-severe interstitial fibrosis and myofibroblastic proliferation. In addition, the lungs showed bilateral panlobar acute bronchopneumonia.

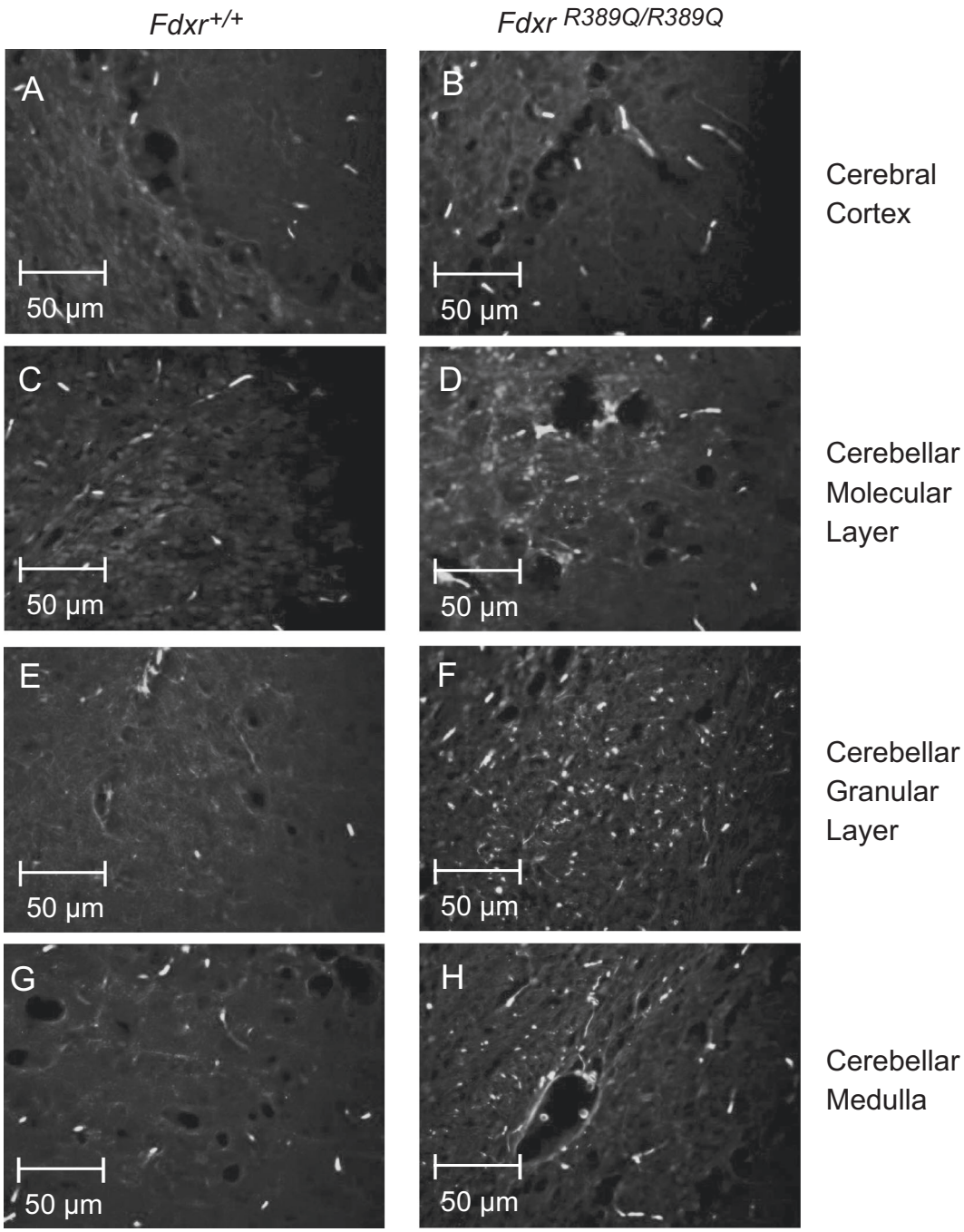

Fig. 5 Neurodegeneration in *Fdxr* mutant mouse brain. Significantly increased immunostaining for Fluoro-Jade C (FJC) was observed in the cerebral cortex **a**–**b**, as well as the molecular layer **c**–**d**, granular layer **e**–**f**, and medullary layer **g**–**h** of the cerebellum

Tissues from occipital cerebral cortex and cerebellar cortex were prepared for light microscopy, transmission electron microscopy, and immunohistochemistry. Hematoxylin and eosin staining of the occipital cerebral cortex indicated loss of neurons in the cortex, and multiple intracellular vacuoles were observed (Fig. 2a–c). Toluidine staining of the cerebral cortex confirmed the presence of the vacuoles (Fig. 2b), and the tissues presented with a spongiform appearance. TEM of the cerebral cortex (Fig. 2c) indicated the presence of multiple large cytoplasmic vacuoles, and the nuclei were displaced. Inside each vacuole, the presence of membranous structures of unknown origin was observed. Similarly, cellular loss was found in the molecular layer, Purkinje cell layer, and granular layer of the cerebellum. Depletion of Purkinje cells, and intracellular vacuoles were observed in the

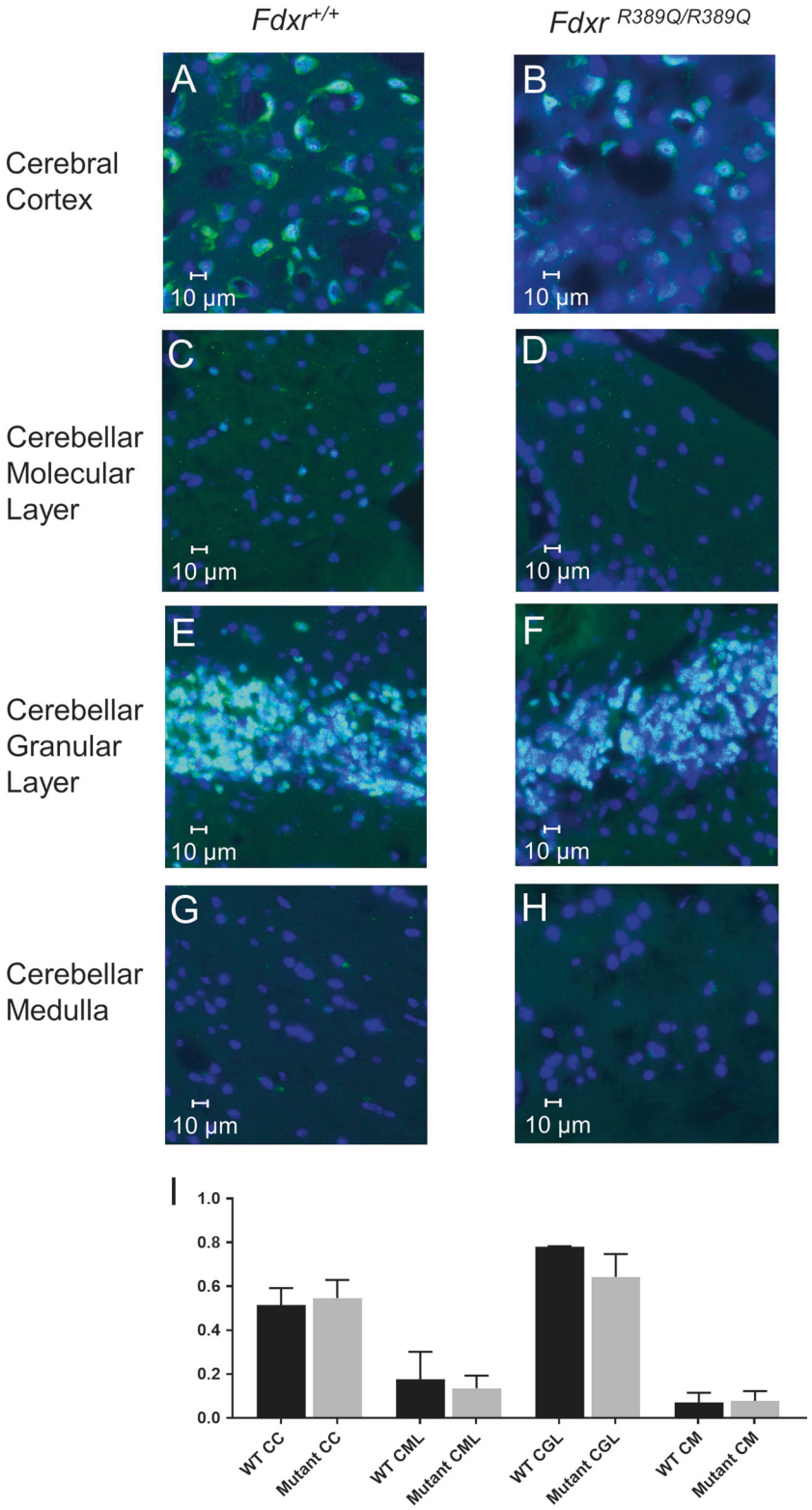

Fig. 6 Modest reduction in the proportion of neurons in *Fdxr* mutant brains. IF staining with anti-NeuN antibody was used to determine the proportion of neurons in mutant and wildtype brains. Counterstaining with DAPI was used to show the total number of cells in each image field; cells staining with DAPI alone are largely composed of glial cells, with a small percentage consisting of neurons such as Purkinje cells that do not express NeuN. Staining reveals a similar number of neurons present in the cerebral cortex **a**–**b**, molecular layer **c**–**d**, and medullary layer **g**–**h** of the cerebellum between *Fdxr* mutant and wildtype mice. The number of neurons present in the granular layer of mutant cerebellar tissue **e**–**f** is modestly, but noticeably reduced relative to wildtype control tissues. The proportion of neurons in each brain region and genotype was also determined by dividing the number of NeuN-positive cells by the total number of DAPI-positive cells **i**, confirming the modest reduction in neurons seen in the granular layer. Cell counts were generated by manual counting of cells in three different fields of view at ×40 magnification, and then averaging the result from the three counts. A total of 174 to 834 cells were counted for each genotype and brain region/layer, which was determined by the density of neurons in each brain region. Abbreviations are as follows: "CC" = Cerebral Cortex, "CML" = Cerebellar Molecular Layer, "CGL" = Cerebellar Granular Layer, "CM" = Cerebellar Medulla, "WT" = Wildtype

cerebellum by H&E (Fig. 2d), toluidine staining (Fig. 2e), and TEM (Fig. 2f). In addition, the spinal cord tissue of the patient was devoid of lower motor neurons, and intracellular vacuoles were also observed (Fig. 2g–i). Furthermore, a biomarker for gliosis and astrocyte activation, GFAP, was markedly increased in tissue samples from mutant brains (Fig. 3a–d). Although not a direct indicator of inflammation, gliosis is often found to be associated with inflammation in

the mammalian brain. Finally, FJC, a widely used marker for neurodegeneration, was found to be expressed at extremely high levels in both the cerebellum and the cerebral cortex (Fig. 3e–h).

Neurodegeneration in the mouse model of *Fdxr*

In order to verify the link between FDXR mutation and neurodegeneration suggested by the patient autopsy tissue, brain sections from the naturally occurring *Fdxr* $^{R389Q/R389Q}$ mutant mouse were stained for the presence of GFAP (Fig. 4). *Fdxr* mutant mice at 10.5 months (Fig. 4b, d, f, h) showed modest but clear increases in the presence of astrocytes in the cerebellum and cerebral cortex in comparison with age-matched wildtype control mice (Fig. 4a, c, e, g). In addition, Bergmann glia in the molecular layer of the cerebellum show stronger GFAP-staining in mutant samples (Fig. 4d) relative to control (Fig. 4c).

To more directly assess neurodegeneration in *Fdxr* mutant mice, brain sections were stained with FJC, a fluorescent high-resolution selective dye for neurodegeneration, as described previously [21]. Degenerative signals were present in axons, dendrites, and several somata of Purkinje cells in *Fdxr* mouse cerebellum at 10.5 months compared with WT controls (Fig. 5). The FJC-positive signals were significantly increased in the cerebral cortex, cerebellar molecular layer, cerebellar granular layer, and cerebellar medulla of *Fdxr* mutant mice at 10.5 months (Fig. 5b, d, f, h) in comparison with age-matched wildtype control mice (Fig. 5a, c, e, g). A parallel analysis of the same brain regions used NeuN to identify the proportion of neurons to non-neuronal cells (Fig. 6a–i). These results indicate a modest loss of neurons in the mutant tissues as compared with wildtype at the 10-month time point, with the greatest difference apparent in the neuron-rich granular layer of the cerebellum. We should point out that many of the degenerating neurons may be able to persist for an extended period in a compromised state before finally succumbing to cell death.

Discussion

Despite the differences in phenotypic severity, both of our patient cases showed core clinical features previously observed with *FDXR* mutations, particularly optic atrophy and some degree of ataxia or abnormal gait. These clinical features are well within the scope of what we have previously documented for FDXR patients [10], leading us to conclude that these patients' conditions are caused by biallelic mutations in the *FDXR* gene. The position of these disease-causing variants within the FDXR protein may provide some insights into their differential severity. The FDXR protein consists of two NAD(P)-binding domain, separated by a FAD/NAD(P)-binding domain. All of the patient variants described here lie within the FAD/NAD(P)-binding domain (Fig. 1f), with the exception of the c.1A > G, p.M1? variant, which is likely to be a null allele due to the loss of the normal start codon. Based on their location, these alleles could affect protein function either by disrupting the protein's ability to transfer electrons from NADPH to FDX1/2, or by destabilizing protein folding or stability. Either outcome would be sufficient to cause the loss of FDXR's critical functions in the cytochrome P450 and iron–sulfur cluster synthesis pathways.

It should be noted that there are several curious features of our two patient cases that merit further investigation. For instance, preterm birth is a distinct feature observed in both cases. However, it is currently unknown whether a fetus carrying FDXR mutations can induce premature labor in an unaffected mother. It should also be noted that the ambiguous genitalia observed in proband 2 is a very unusual phenomenon. At this moment, we cannot reliably link this particular phenotype to the *FDXR* mutation. However, mutations of FDXR may interfere with cholesterol-related hormone synthesis and/or metabolism due to its involvement in with mitochondrial cytochrome P450.

Compared with the severe gliosis observed in the patient tissues shown in Fig. 3, the increase in gliosis observed in the naturally occurring homozygous p.R389Q mouse mutant [22] (Fig. 4) is much more subtle, perhaps reflective of a lower level of severity for the mouse variant. This is in line with our previous results with p.R389Q, which corresponds to the site of the most common p.R392W variant observed in humans. This allele, which broadly recapitulates the mitochondrial dysfunctions and peripheral neurodegeneration observed in our patient population, nevertheless shows a generally less-severe phenotype than would be expected based on the human variant [10]. This may be related to the fact that arginine to glutamine substitutions are generally less disruptive to protein function than arginine to tryptophan substitutions, and a closer examination of this question with a CRISPR-generated R389W allele is likely warranted. Still, the fact remains that the phenotype of the mouse mutant broadly matches those observed in our patient population, providing strong confirmation of the causal role of *FDXR* mutations in optic atrophy and neuropathy.

Prior work in the p.R389Q mouse model has already established that mutation of *Fdxr* leads to peripheral neuropathy and optic atrophy. Our histological analysis of mouse and patient brain tissues serves as a confirmation that mutation of *Fdxr* also mediates neurodegeneration in the brain. Markers of inflammation/gliosis (GFAP) and neurodegeneration (FJC) both showed increased expression in

cerebellum and cerebral cortex tissue of *Fdxr* mutants relative to age-matched controls from the same background.

Inappropriate accumulation of iron (in the form of mitochondrial iron overload) has already been demonstrated to be a feature of FDXR dysfunction [14], and it will be worthwhile to explore in further detail the role that iron overload plays in the extensive neurodegeneration observed in both our patients and in the *Fdxr* mutant mice. There is, of course, already established precedence for defects in iron metabolism causing neurodegerative effects. Friedreich's ataxia, a hereditary ataxia caused by trinucleotide repeat expansion in the Fe–S cluster synthesis protein frataxin [23–25], has been shown to cause atrophy of the cerebellar dentate nucleus [26]. Elevated iron levels have also been found in dopaminergic neurons of patients with Parkinson's disease [27]. Perhaps most intriguingly, early-stage Parkinson's patients treated with the iron chelator deferiprone have shown significant improvements (relative to placebo-treated patients) in a pilot clinical trial [28]. A subsequent phase 2 trial in a larger sample of Parkinson's patients indicates that deferiprone can produce significant reductions in iron levels in at least some of the relevant regions of the brain, whereas causing little detrimental effect on cognitive function or quality of life [29]. Other studies have confirmed that deferiprone can halt or delay the progression of other forms of neurodegenerative disease such as Pantothenate kinase-associated neurodegeneration [30] and Friedreich's ataxia [31–33]. As iron accumulation and overload is likely to be a major disease mechanism for mutations in iron–sulfur cluster genes like *FDXR*, there may be value in expanding the use of the treatment to these related diseases in the future. To this end, we are currently in the early phases of investigating the efficacy of deferiprone-based chelation therapy in the *Fdxr* mouse, particularly the effect of the treatment on both gliosis (as a proxy for inflammation) and the neurodegenerative process.

In this paper, we have examined two new human cases of FDXR mutation and the *Fdxr* mouse model to expand our understanding of the pathology of *FDXR*-mediated disease. Our results suggest that inflammation could be a major component of pathology in neurodegeneration. As such, these findings are likely to be generalizable to other forms of neurodegenerative disease. Further investigation of the *Fdxr* mouse model will provide valuable insights for developing treatments for mitochondrial dysfunction-related neurodegeneration.

Acknowledgements We thank the patient families for their participation in this study. We also thank Jun-Song Mo, Geogianne M. Ciraolo and Tilat Rizvi and Jun-Song Mo at Cincinnati Children's Hospital for their help obtaining the electron microscopy images. This work was supported in part by Cincinnati Children's Hospital Research Foundation and National Eye Institute (1R01EY026609-01 awarded to TH). Animal studies were supported by in part by The Jackson Laboratory and by the NIH Office of Research Infrastructure Programs (R24 OD021325-01 awarded to L.G.R).

Compliance with ethical standards

Conflict of interest The authors declare no conflict of interest. A.C. is a full-time employee of Ambry Genetics.

References

1. Shoffner JM, Lott MT, AMS Lezza, Seibel P, Ballinger SW, Wallace DC. Myoclonic epilepsy and ragged-red fiber disease (MERRF) is associated with a mitochondrial DNA tRNALys mutation. Cell. 1990;61:931–7.
2. Nijtmans LG, Henderson NS, Attardi G, Holt IJ. Impaired ATP synthase assembly associated with a mutation in the human ATP synthase subunit 6 gene. J Biol Chem. 2001;276:6755–62.
3. Goto Y, Nonaka I, Horai S. A mutation in the tRNA(Leu)(UUR) gene associated with the MELAS subgroup of mitochondrial encephalomyopathies. Nature. 1990;348:651–3.
4. Wallace DC. A mitochondrial paradigm of metabolic and degenerative diseases, aging, and cancer: a dawn for evolutionary medicine. Annu Rev Genet. 2005;39:359–407.
5. Webert H, Freibert SA, Gallo A, Heidenreich T, Linne U, Amlacher S, et al. Functional reconstitution of mitochondrial Fe/S cluster synthesis on Isu1 reveals the involvement of ferredoxin. Nat Commun. 2014;5:5013.
6. Paul VD, Lill R. Biogenesis of cytosolic and nuclear iron-sulfur proteins and their role in genome stability. Biochim Biophys Acta. 2015;1853:1528–39.
7. Lim SC, Friemel M, Marum JE, Tucker EJ, Bruno DL, Riley LG, et al. Mutations in LYRM4, encoding iron-sulfur cluster biogenesis factor ISD11, cause deficiency of multiple respiratory chain complexes. Hum Mol Genet. 2013;22:4460–73.
8. Di Fonzo A, Ronchi D, Lodi T, Fassone E, Tigano M, Lamperti C, et al. The mitochondrial disulfide relay system protein GFER is mutated in autosomal-recessive myopathy with cataract and combined respiratory-chain deficiency. Am J Hum Genet. 2009;84:594–604.
9. Martelli A, Puccio H. Dysregulation of cellular iron metabolism in Friedreich ataxia: from primary iron-sulfur cluster deficit to mitochondrial iron accumulation. Front Pharmacol. 2014;5:130.
10. Peng Y, Shinde DN, Valencia CA, Mo JS, Rosenfeld J, Truitt Cho M, et al. Biallelic mutations in the ferredoxin reductase gene cause novel mitochondriopathy with optic atrophy. Hum Mol Genet. 2017;26:4937–50.
11. Paul A, Drecourt A, Petit F, Deguine DD, Vasnier C, Oufadem M, et al. FDXR mutations cause sensorial neuropathies and expand the spectrum of mitochondrial Fe-S-synthesis diseases. Am J Hum Genet. 2017;101:630–7.
12. Hwang PM, Bunz F, Yu J, Rago C, Chan TA, Murphy MP, et al. Ferredoxin reductase affects p53-dependent, 5-fluorouracil-induced apoptosis in colorectal cancer cells. Nat Med. 2001;7:1111–7.
13. Solish SB, Picado-Leonard J, Morel Y, Kuhn RW, Mohandas TK, Hanukoglu I, et al. Human adrenodoxin reductase: two mRNAs encoded by a single gene on chromosome 17cen----q25 are expressed in steroidogenic tissues. Proc Natl Acad Sci USA. 1988;85:7104–8.
14. Shi Y, Ghosh M, Kovtunovych G, Crooks DR, Rouault TA. Both human ferredoxins 1 and 2 and ferredoxin reductase are important for iron-sulfur cluster biogenesis. Biochim Biophys Acta. 2012;1823:484–92.

15. Sheftel AD, Stehling O, Pierik AJ, Elsasser HP, Muhlenhoff U, Webert H, et al. Humans possess two mitochondrial ferredoxins, Fdx1 and Fdx2, with distinct roles in steroidogenesis, heme, and Fe/S cluster biosynthesis. Proc Natl Acad Sci USA. 2010;107:11775–80.
16. Cai K, Tonelli M, Frederick RO, Markley JL. Human mitochondrial ferredoxin 1 (FDX1) and ferredoxin 2 (FDX2) both bind cysteine desulfurase and donate electrons for iron-sulfur cluster biosynthesis. Biochemistry. 2017;56:487–99.
17. Hanukoglu I, Jefcoate CR. Mitochondrial cytochrome P-450scc. Mechanism of electron transport by adrenodoxin. J Biol Chem. 1980;255:3057–61.
18. Zanger UM, Schwab M. Cytochrome P450 enzymes in drug metabolism: regulation of gene expression, enzyme activities, and impact of genetic variation. Pharmacol Ther. 2013; 138:103–41.
19. Hanukoglu I. Steroidogenic enzymes: structure, function, and role in regulation of steroid hormone biosynthesis. J Steroid Biochem Mol Biol. 1992;43:779–804.
20. Tanaka AJ, Cho MT, Millan F, Juusola J, Retterer K, Joshi C, et al. Mutations in SPATA5 are associated with microcephaly, intellectual disability, seizures, and hearing loss. Am J Hum Genet. 2015;97:457–64.
21. Li Z, Peng Y, Hufnagel RB, Hu YC, Zhao C, Queme LF, et al. Loss of SLC25A46 causes neurodegeneration by affecting mitochondrial dynamics and energy production in mice. Hum Mol Genet. 2017;26:3776–91.
22. Fairfield H, Srivastava A, Ananda G, Liu R, Kircher M, Lakshminarayana A, et al. Exome sequencing reveals pathogenic mutations in 91 strains of mice with Mendelian disorders. Genome Res. 2015;25:948–57.
23. Campuzano V, Montermini L, Molto MD, Pianese L, Cossee M, Cavalcanti F, et al. Friedreich's ataxia: autosomal recessive disease caused by an intronic GAA triplet repeat expansion. Science. 1996;271:1423–7.
24. Rotig A, de Lonlay P, Chretien D, Foury F, Koenig M, Sidi D, et al. Aconitase and mitochondrial iron-sulphur protein deficiency in Friedreich ataxia. Nat Genet. 1997; 17:215–7.
25. Cavadini P, O'Neill HA, Benada O, Isaya G. Assembly and iron-binding properties of human frataxin, the protein deficient in Friedreich ataxia. Hum Mol Genet. 2002;11:217–27.
26. Solbach K, Kraff O, Minnerop M, Beck A, Schöls L, Gizewski ER, et al. Cerebellar pathology in Friedreich's ataxia: Atrophied dentate nuclei with normal iron content. NeuroImage Clin. 2014;6:93–9.
27. Oakley AE, Collingwood JF, Dobson J, Love G, Perrott HR, Edwardson JA, et al. Individual dopaminergic neurons show raised iron levels in Parkinson disease. Neurology. 2007;68:1820–5.
28. Devos D, Moreau C, Devedjian JC, Kluza J, Petrault M, Laloux C, et al. Targeting chelatable iron as a therapeutic modality in Parkinson's disease. Antioxid Redox Signal. 2014;21:195–210.
29. Martin-Bastida A, Ward RJ, Newbould R, Piccini P, Sharp D, Kabba C, et al. Brain iron chelation by deferiprone in a phase 2 randomised double-blinded placebo controlled clinical trial in Parkinson's disease. Sci Rep. 2017;7:1398.
30. Abbruzzese G, Cossu G, Balocco M, Marchese R, Murgia D, Melis M, et al. A pilot trial of deferiprone for neurodegeneration with brain iron accumulation. Haematologica. 2011;96:1708–11.
31. Velasco-Sanchez D, Aracil A, Montero R, Mas A, Jimenez L, O'Callaghan M, et al. Combined therapy with idebenone and deferiprone in patients with Friedreich's ataxia. Cerebellum. 2011;10:1–8.
32. Pandolfo M, Arpa J, Delatycki MB, Le Quan Sang KH, Mariotti C, Munnich A, et al. Deferiprone in Friedreich ataxia: a 6-month randomized controlled trial. Ann Neurol. 2014;76:509–21.
33. Elincx-Benizri S, Glik A, Merkel D, Arad M, Freimark D, Kozlova E, et al. Clinical experience with deferiprone treatment for friedreich ataxia. J Child Neurol. 2016;31:1036–40.
34. Hulo N, Bairoch A, Bulliard V, Cerutti L, Cuche BA, de Castro E, et al. The 20 years of PROSITE. Nucleic Acids Res. 2008;36: D245–D9.